Hindawi
International Journal of Aerospace Engineering
Volume 2022, Article ID 1862392, 17 pages
https://doi.org/10.1155/2022/1862392

Research Article

A Passive Vibration Control Method of Modular Space Structures Based on Band Gap Optimization

Juntao Zhu, Tuanjie Li, Bo Li, Yaqiong Tang, Zuowei Wang, and Qingjuan Duan

School of Mechano-Electronic Engineering, Xidian University, Xi'an 710071, China

Correspondence should be addressed to Tuanjie Li; tjli@mail.xidian.edu.cn

Received 17 July 2022; Revised 5 August 2022; Accepted 26 August 2022; Published 9 September 2022

Academic Editor: Jinchao Chen

Modular space structure has become a research hotspot in the aerospace field. In the microgravity and weak damping space environment, modular space structures may continuously vibrate due to the transient excitation caused by satellite attitude adjustment or space debris impact, which will make the structure unstable. Therefore, a passive vibration control method based on band gap design is proposed for the modular space structures. Firstly, a modular spectral element model based on the super element is established, and the modular spectral element model is expanded into modular space structures. Then, band gap characteristics of the modular space structure are analyzed and optimized to improve the wave isolation ability. The numerical simulation shows that the elastic wave in the band gap can be effectively isolated and the band gap is significantly improved by optimizing structural parameters.

1. Introduction

Deployable space structures have been widely used in aerospace due to the advantages of lightweight and large ratio of deployed and folded volumes. With the development toward large-scale, high-precision, and on-orbit assembling [1], the modularization structure has become a popular structural form for deployable space structures. Modular space structures belong to a class of dynamical systems with weak damping and large flexibility. It is well known that this type of system will continuously vibrate under complex space environments, such as the transient excitation caused by satellite attitude adjustment or space debris impact. Therefore, control methods [2–5] must be considered to eliminate the vibration.

For space structures, the vibration control method can be divided into two categories: active and passive control. Active control [6–8] introduces an automatic control system with an additional power supply to dampen the vibration amplitude. It can provide optimal vibration control effect under some specific conditions, but the control system is complex, and it is hard to obtain enough power in space. Passive control, in contrast, needs no additional power supply, and it has the advantages of low cost, high reliability, broadband vibration reduction, and so on.

So far, some scholars have investigated the passive control methods for space structures. Bishop and Striz [9] studied an optimal configuration method of viscous dampers for a modular frame structure based on the genetic algorithm. Xu et al. [10] proposed a hybrid optimization model combining the evolutionary algorithm with the simulated annealing algorithm to solve the configuration problem of viscoelastic dampers. Kim et al. [11] investigated a magnetorheological (MR) damper-based intelligent passive control system for mitigating the vibration of stay cables. It was found that the vibration reduction effect was slightly better than conventional MR dampers. Tong and Zhao [12] investigated the optimization of multiple tuned mass dampers (TMDs) to reduce vibrations of flexible structures. Preumont et al. [13] studied the vibration reduction analysis of the modular frame structure based on the piezoelectric vibration absorber. It can be found that the damping vibration reduction with surface damping layers [14], discrete dampers, and vibration absorbers [15] has been widely used in space structures. However, the damping vibration reduction needs to be equipped with many dampers to achieve a

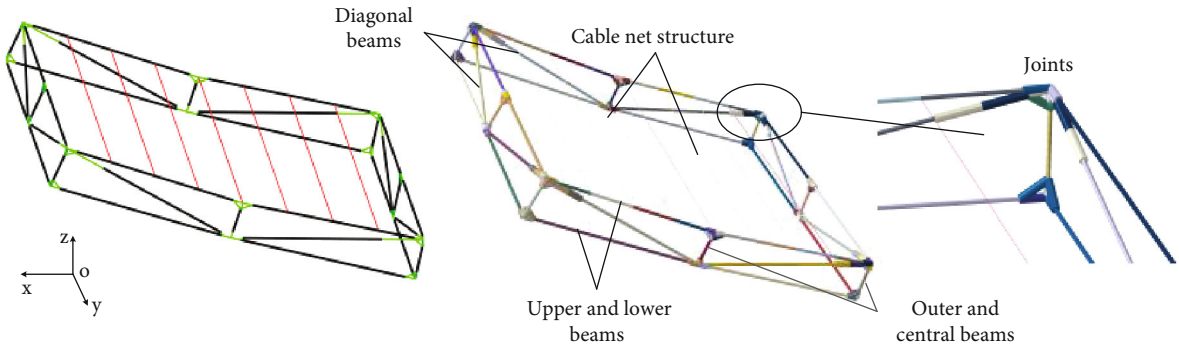

Figure 1: Basic unit structure of modular space structures.

better control effect, which will increase the additional mass of the system.

It is noted that modular space structures have the property of periodic arrays, that is, band gaps. That is to say, we can optimize the structure material and geometric parameters to tune the position and width of the band gaps so that the self-vibration-suppression capability can be improved [16]. Inspired by this, we take the basic unit of modular space structures as a super element composed of various materials so that we can improve the elastic wave isolation ability by artificially optimizing the band gap.

At present, the band gap of periodic structures can be analyzed by the finite element method (FEM) [17, 18], the finite difference method [19], the plane wave expansion method [20], the traveling wave method [21], the transfer matrix method [22], the spectral element method (SEM) [23–26], etc. Thereinto, SEM is proposed and applied to truss-type space structures by U. Lee and J. Lee [27]. Dutkiewicz and Machado [28] analyzed vibrations of an overhead transmission line in a damping environment. Jeong et al. [29] investigated the vibration analysis of a multispan beam subjected to a moving point force by SEM. The SEM has the advantages of low computational cost and accurate calculation results. So, the SEM is used to build the dynamic model for the gap band analysis of modular space structures.

However, in the optimization iteration process, a large number of frequencies need to be calculated over and over again, which results in a huge amount of computation. What is worse, there are too many structural parameters to optimize the gap band effectively. Therefore, a super element model is first established and grouped for modular structures to obtain a fast and accurate calculation. Then, sensitivity analysis is carried out to select sensitive parameters and eliminate invalid design variables for the band gap optimization model. Compared with traditional damping vibration reduction methods, the proposed method realizes the vibration control without additional mass and cost. This paper provides a new idea for the vibration control of the modular space structure.

The remainder of this paper is organized as follows. Section 2 introduces the basic unit of modular space structures. In Section 3, the basic unit is taken as a super element, and its dynamic spectral element model is established. Section 4 reveals band gap characteristics of modular space structures. In Section 5, the band gap is optimized to improve the wave isolation ability of modular space structures. Some conclusions are summarized in Section 6.

2. Problem Statement

As shown in Figure 1, the basic unit structure of modular space structures is mainly composed of upper beams, lower beams, outer and central beams, diagonal beams, joints, and the cable net structure. The modular space structure is formed by a basic module structure through the periodic array, which is a form of the periodic structure. Periodic structures have band gap characteristics [26], and the propagation of elastic waves is prohibited within a certain frequency band. The band gap characteristic of the periodic structure is related to the structure's material and geometry properties and the number of periods. So, the modular space structure can exhibit different characteristics of band gaps of elastic wave propagation, by adjusting the magnitude of cross-section, structure dimension, and pretensions of the element. To effectively reveal the characteristics of elastic wave propagation of this complex structure, we derive the spectral element matrixes of the 3D cable and beam elements and the dynamic spectral element model of the basic unit based on SEM. The basic unit structure is the smallest repeating unit in the modular space structure, as shown in Figure 1. Then, to reduce the calculation, the super element of the basic unit structure can be obtained by the dimension reduction process. Finally, the spectral element model of the modular space structure can be obtained by periodically expanding the super element according to the topological connection relationship.

3. Spectral Element Method

3.1. Spectral Element Matrix for 3D Beams. In this paper, the spectral element matrix of the beam element is derived based on the Euler-Bernoulli beam assumptions. The assumption is that the additional deflection changes caused by shear deformation are not considered. According to the theoretical analysis of the Euler-Bernoulli beam and the force-displacement relationship [20], the spectral finite element equation for the flexural motion of the beam can be

obtained as

$$\begin{Bmatrix} Q_i \\ M_i \\ Q_j \\ M_j \end{Bmatrix} = \frac{EI_y}{L^3} \begin{bmatrix} S_{B11} & S_{B12} & S_{B13} & S_{B14} \\ S_{B21} & S_{B22} & S_{B23} & S_{B24} \\ S_{B31} & S_{B32} & S_{B33} & S_{B34} \\ S_{B41} & S_{B42} & S_{B43} & S_{B44} \end{bmatrix} \begin{Bmatrix} W_i \\ \Phi_i \\ W_j \\ \Phi_j \end{Bmatrix} = \frac{EI_y}{L^3} S_B(k_F, L)^T d = S_B(\omega) d, \tag{1}$$

where $\{Q_i\, M_i\, Q_j\, M_j\}^T$ is the generalized force vector, Q_i and Q_j are cross forces of nodes, and M_i and M_j are moments of the beam element. $\{W_i\, \Phi_i\, W_j\, \Phi_j\}^T$ is the displacement vector, W_i and W_j are spectral node displacements, and Φ_i and Φ_j are cross-section corner of the beam element. E is the elastic modulus, I_y is the sectional area moment of inertia about the neutral axis, L is the length of the beam element, and $S_B(\omega)$ is the spectral element stiffness matrix of the flexural wave of 3D beams, which characterizes the relationship of the flexural wave between displacement and force in the frequency domain. The subitems of $S_B(\omega)^T$ are

$$\begin{aligned} S_{B11} &= S_{B33} = \Delta_B \bar{L}^3 \left(\cos \bar{L} \bullet \sinh \bar{L} + \sin \bar{L} \bullet \cosh \bar{L}\right), \\ S_{B22} &= S_{B44} = \Delta_B \bar{L}^3 k_F^{-2} \left(\sin \bar{L} \bullet \cosh \bar{L} - \cos \bar{L} \bullet \sinh \bar{L}\right), \\ S_{B12} &= -S_{B34} = \Delta_B \bar{L}^3 k_F^{-1} \sin \bar{L} \bullet \sinh \bar{L}, \\ S_{B13} &= -\Delta_B \bar{L}^3 \left(\sin \bar{L} + \sinh \bar{L}\right), \\ S_{B14} &= -S_{B23} = \Delta_B \bar{L}^3 k_F^{-1} \left(-\cos \bar{L} + \cosh \bar{L}\right), \\ S_{B24} &= \Delta_B \bar{L}^3 k_F^{-2} \left(-\sin \bar{L} + \sinh \bar{L}\right), \\ \Delta_B &= \frac{1}{\left(1 - \cos \bar{L} \bullet \cosh \bar{L}\right)}, \\ \bar{L} &= k_F L, \end{aligned} \tag{2}$$

where $k_F = \sqrt[4]{\omega^2 \rho A / EI_z}$ is the wave number of the flexural motion of the beam.

The longitudinal motion can be obtained as

$$\begin{Bmatrix} N_i \\ N_j \end{Bmatrix} = \frac{EA}{L} \begin{bmatrix} k_L L \cot(k_L L) & -k_L L \csc(k_L L) \\ -k_L L \csc(k_L L) & k_L L \cot(k_L L) \end{bmatrix} \begin{bmatrix} U_i \\ U_j \end{bmatrix} = \frac{EA}{L} S_R(k_L, L)^T d = S_R(\omega) d, \tag{3}$$

where N_i and N_j are the nodal longitudinal forces. U_i and U_j are the nodal longitudinal displacements. $k_L = \sqrt{\omega^2 \rho A / EA}$ is the wave number for the longitudinal motion, ρ is the mass density, A is the sectional area, and $S_R(\omega)$ is the spectral element stiffness matrix of the longitudinal wave of 3D beams, which characterizes the relationship of the longitudinal wave between displacement and force in the frequency domain.

The torsional motion can be obtained as

$$\begin{Bmatrix} T_i \\ T_j \end{Bmatrix} = \frac{GI_P}{L} \begin{bmatrix} k_T L \cot(k_T L) & -k_T L \csc(k_T L) \\ -k_T L \csc(k_T L) & k_T L \cot(k_T L) \end{bmatrix} \begin{bmatrix} \Phi_i \\ \Phi_j \end{bmatrix} = \frac{GI_P}{L} S_T(k_T, L)^T d = S_T(\omega) d, \tag{4}$$

where T_i and T_j are the nodal torsional moments. Φ_i and Φ_j are the nodal torsional angles, and $G = E/(2(1+\mu))$ is the shear modulus, μ is the Poisson's ratio, I_P is the polar moment of inertia, and $k_T = \sqrt{\omega^2 \rho I_P / GI_P}$ is the wave number for the torsional motion, and $S_T(\omega)$ is the spectral element stiffness matrix of the torsional wave of 3D beams, which characterizes the relationship of the torsional wave between displacement and force in the frequency domain.

The spectral element matrix of 3D beam elements can be obtained by assembling longitudinal, torsional, and flexural spectral element matrixes of the Euler-Bernoulli beam as

$$S_B^L(\omega) d_B^L = F_B^L, \tag{5}$$

where $S_B^L(\omega)$ is the spectral element stiffness matrix of the 3D beams in the element coordinate system, and it can also be written as

$$S_B^L(\omega) = \begin{bmatrix} S_{B11}^L & S_{B12}^L \\ \text{sym} & S_{B22}^L \end{bmatrix}, \tag{6}$$

where S_{B11}^L, S_{B12}^L, and S_{B22}^L can be expressed as

$$S_{B11}^L = \begin{bmatrix} S_{R11} & 0 & 0 & 0 & 0 & 0 \\ 0 & S_{B11} & 0 & 0 & 0 & S_{B12} \\ 0 & 0 & S_{B11} & 0 & -S_{B12} & 0 \\ 0 & 0 & 0 & S_{T11} & 0 & 0 \\ 0 & 0 & -S_{B12} & 0 & S_{B22} & 0 \\ 0 & S_{B21} & 0 & 0 & 0 & S_{B22} \end{bmatrix}, \tag{7}$$

$$S_{B12}^{L} = \begin{bmatrix} S_{R12} & 0 & 0 & 0 & 0 & 0 \\ 0 & S_{B13} & 0 & 0 & 0 & S_{B14} \\ 0 & 0 & S_{B13} & 0 & -S_{B14} & 0 \\ 0 & 0 & 0 & S_{T12} & 0 & 0 \\ 0 & 0 & -S_{B23} & 0 & S_{B24} & 0 \\ 0 & S_{B23} & 0 & 0 & 0 & S_{B24} \end{bmatrix}, \quad (8)$$

$$S_{B22}^{L} = \begin{bmatrix} S_{R22} & 0 & 0 & 0 & 0 & 0 \\ 0 & S_{B33} & 0 & 0 & 0 & S_{B34} \\ 0 & 0 & S_{B33} & 0 & -S_{B34} & 0 \\ 0 & 0 & 0 & S_{T22} & 0 & 0 \\ 0 & 0 & -S_{B43} & 0 & S_{B44} & 0 \\ 0 & S_{B43} & 0 & 0 & 0 & S_{B44} \end{bmatrix}, \quad (9)$$

where S_{Rij} and $S_{Tij}(i, j = 1, 2)$ are the subitems of the spectral element stiffness matrixes of longitudinal and torsional motion of the Euler-Bernoulli beam, respectively, and S_{Bij} $(i, j = 1, 2, 3, 4)$ is the subitems of the spectral element stiffness matrix of flexural motion of the Euler-Bernoulli beam.

The spectral element matrix of the 3D beams in the global coordinate system can be obtained by transformation of coordinates as

$$S_B^G(\omega) = T_r^T S_B^L(\omega) T_r, \quad (10)$$

where T_r is the coordinate transformation matrix and $S_B^G(\omega)$ is the total spectral element stiffness matrix of 3D beams in global coordinate system.

3.2. Spectral Element Matrix for 3D Cables. Cables involved in the cable net structure are simulated by strings of which the longitudinal vibration equation of the tension cable is consistent with the Bernoulli-Euler beam. The spectral element equation of the transverse vibration of the tension cable can be given as follows.

$$\begin{Bmatrix} H_i \\ H_j \end{Bmatrix} = \frac{T}{L} \begin{bmatrix} k_{CT}L \cot(k_{CT}L) & -k_{CT}L \csc(k_{CT}L) \\ -k_{CT}L \csc(k_{CT}L) & k_L L \cot(k_{CT}L) \end{bmatrix} \begin{bmatrix} W_i \\ W_j \end{bmatrix} = \frac{T}{L} S_{CT}(k_{CT}, L)^T d = S_{CT}(\omega) d, \quad (11)$$

where H_i and H_j are the nodal transverse forces. W_i and W_j are the nodal transverse displacements. $k_{CT} = \sqrt{\omega^2 \rho A / T}$ is the wave number of the transverse motion. T is the pretension, which provides the transverse stiffness of the tension cable. $S_{CT}(\omega)$ is the spectral element stiffness matrix of the transverse wave of 3D cables, which characterizes the transverse motion relationship of 3D cables between displacement and force in the frequency domain. The subitems of $S_{CT}(\omega)^T$ are

$$\begin{aligned} S_{CT11} &= S_{CT22} = (k_{CT}L) \cot(k_{CT}L), \\ S_{CT12} &= S_{CT21} = -(k_{CT}L) \csc(k_{CT}L). \end{aligned} \quad (12)$$

The spectral element stiffness matrix of 3D cables can be obtained by assembling the transverse and longitudinal spectral element matrixes as

$$S_C^L(\omega) d_C^L = F_C^L, \quad (13)$$

where $S_C^L(\omega)$ is the spectral element stiffness matrix of the 3D cables, and it can also be written as

$$S_C^L(\omega) = \begin{bmatrix} S_{C11}^L & S_{C12}^L \\ \text{sym} & S_{C22}^L \end{bmatrix}, \quad (14)$$

where S_{C11}^L, S_{C12}^L, and S_{C22}^L can be expressed as

$$S_{C11}^L = \begin{bmatrix} S_{R11} & 0 & 0 \\ 0 & S_{CT11} & 0 \\ 0 & 0 & S_{CT11} \end{bmatrix}, \quad S_{C12}^L = \begin{bmatrix} S_{R12} & 0 & 0 \\ 0 & S_{CT12} & 0 \\ 0 & 0 & S_{CT12} \end{bmatrix}, \quad S_{C22}^L = \begin{bmatrix} S_{R22} & 0 & 0 \\ 0 & S_{CT22} & 0 \\ 0 & 0 & S_{CT22} \end{bmatrix}, \quad (15)$$

where S_{Rij} and $S_{CTij}(i, j = 1, 2)$ are the subitems of the spectral element matrixes of longitudinal and transverse motion of the tension cable, respectively.

The spectral element matrix of the 3D cables in the global coordinate system can be obtained by transformation of coordinates as

$$S_C^G(\omega) = T_r^T S_C^L(\omega) T_r, \quad (16)$$

where T_r^T is the coordinate transformation matrix and $S_C^G(\omega)$ is the total spectral element stiffness matrix of 3D cables in global coordinate system.

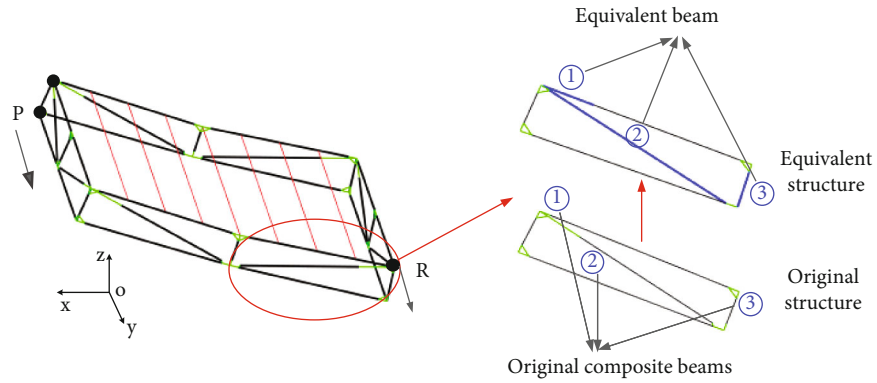

Figure 2: Equivalent super element.

Table 1: Material parameters.

Properties	Frame	Joints	Cable net
Material type	Carbon fiber	Aluminum alloy	Aramid fiber
Section type	Hollow circle section	Solid circle section	Solid circle section
Radius (m)	Outer diameter 0.015 Inside diameter 0.0135	0.03	0.001
Elastic modulus (GPa)	370	72	20
Poisson's ratio	0.3	0.33	0.3
Density (kg/m^3)	1800	2730	1450
Pretension (N)	0	0	1

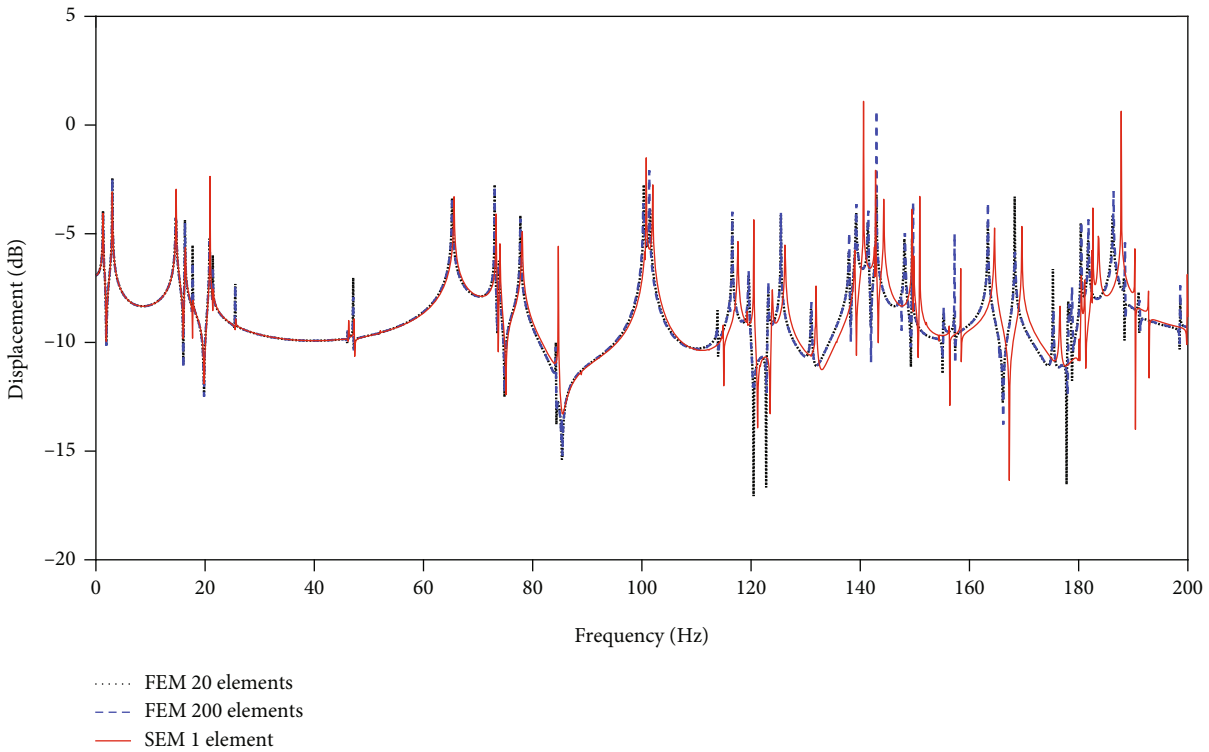

Figure 3: Frequency response comparison between FEM and SEM.

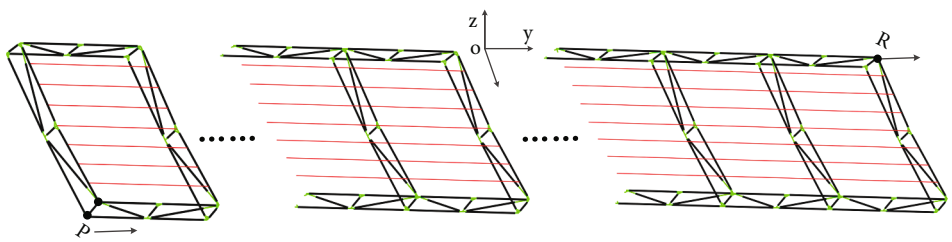

Figure 4: Modular space structure.

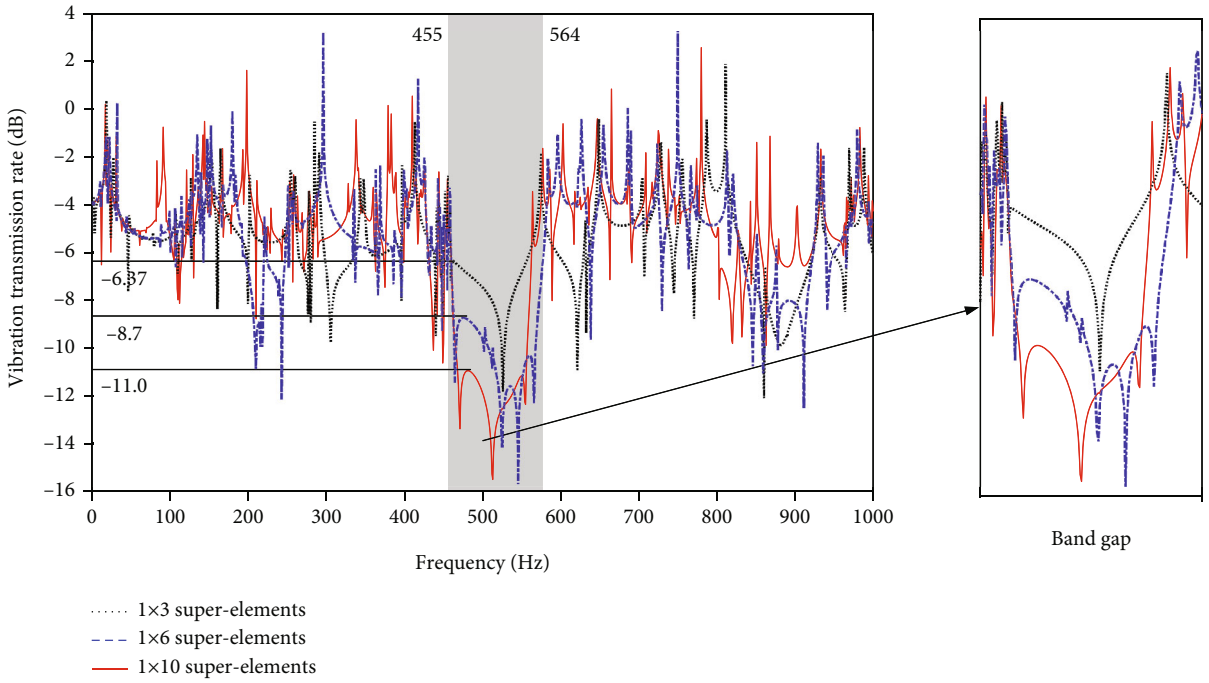

Figure 5: Vibration transmission rate of node R of the modular space structure.

3.3. Spectral Element Matrix of the Super Element. In order to improve computational efficiency, a degree reduction method is used to reduce the dimensionality of the spectral element matrix. As shown in Figure 2, the internal nodes of original composite beams ② can be presented by two end nodes. The spectral element equation of original composite beams ② in the global coordinate system can be written as

$$\begin{bmatrix} \bar{S}_{B2ii} & \bar{S}_{B2ij} \\ \bar{S}_{B2ji} & \bar{S}_{B2jj} \end{bmatrix} \begin{Bmatrix} \bar{d}_i \\ \bar{d}_j \end{Bmatrix} = \begin{Bmatrix} \bar{f}_i \\ 0 \end{Bmatrix}, \tag{17}$$

where $\bar{d}_i$ and $\bar{d}_j$ are the boundary and internal nodal displacements of original composite beams ②, respectively, and $\bar{f}_i$ is the boundary force vector.

According to the principle of condensation, the equivalent beam ② can be deduced as

$$\bar{S}^G_{B2}(\omega)\bar{d} = \bar{f}, \tag{18}$$

where the spectral element matrix of equivalent beam ② is

$$\bar{S}^G_{B2}(\omega) = \bar{S}_{B2ii} - \bar{S}_{B2ij}\left(\bar{S}_{B2jj}\right)^{-1}\bar{S}_{B2ji}. \tag{19}$$

The spectral element matrixes of equivalent beams ① and ③ are similar to that of the equivalent beam ② and can be shown as

$$\bar{S}^G_{Bn}(\omega) = \bar{S}_{Bnii} - \bar{S}_{Bnij}\left(\bar{S}_{Bnjj}\right)^{-1}\bar{S}_{Bnji}\ (n = 1, 3). \tag{20}$$

Specifying material parameters of the super element shown in Table 1 and applying the displacement excitation

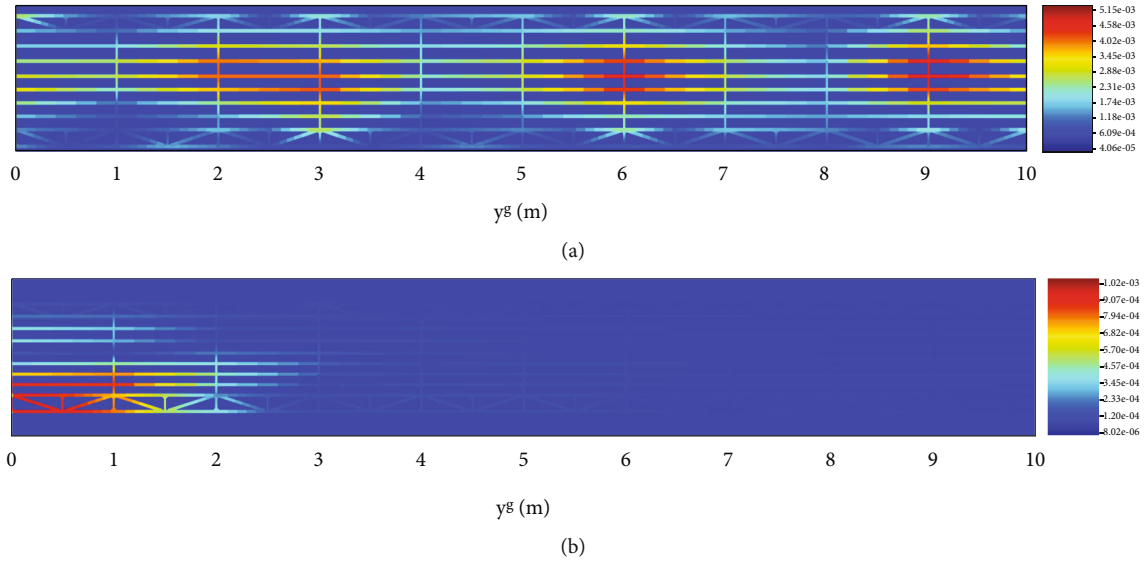

Figure 6: Vibration distributions of the modular space structure: (a) $f = 400$ Hz; (b) $f = 500$ Hz.

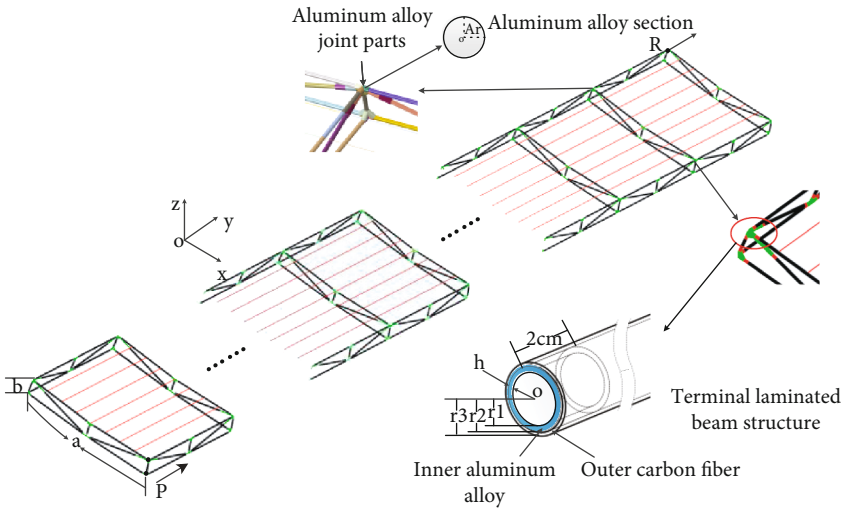

Figure 7: Structural details of the modular space structure.

$d = 0.001e^{i\omega t}$ m at node P, we can obtain the frequency response at node R by solving the spectral element model. The comparisons of the results obtained by the finite element simulation with our numerical results are shown in Figure 3.

It is found that the results of FEM are almost consistent with SEM from 0 to 100 Hz, while they gradually deviate from 100 Hz to 200 Hz. The reason for this difference is that FEM has truncation errors if the refined mesh number is insufficient, while SEM uses the precise wave solution in the frequency domain. Compared with FEM, SEM has no truncation error, so it can obtain accurate calculation results with a smaller number of elements, thereby reducing the amount of calculation and improving the calculation efficiency.

4. Band Gap Analysis of Modular Space Structure

The super element can be used as the basic element to expand into a periodic structure. The vibration transmission rate is defined as Equation (21) and used to evaluate the attenuation characteristics of the periodic structure.

$$T = \lg\left(\frac{w_0}{w_i}\right), \tag{21}$$

where w_0 and w_i are the output and input displacements, respectively.

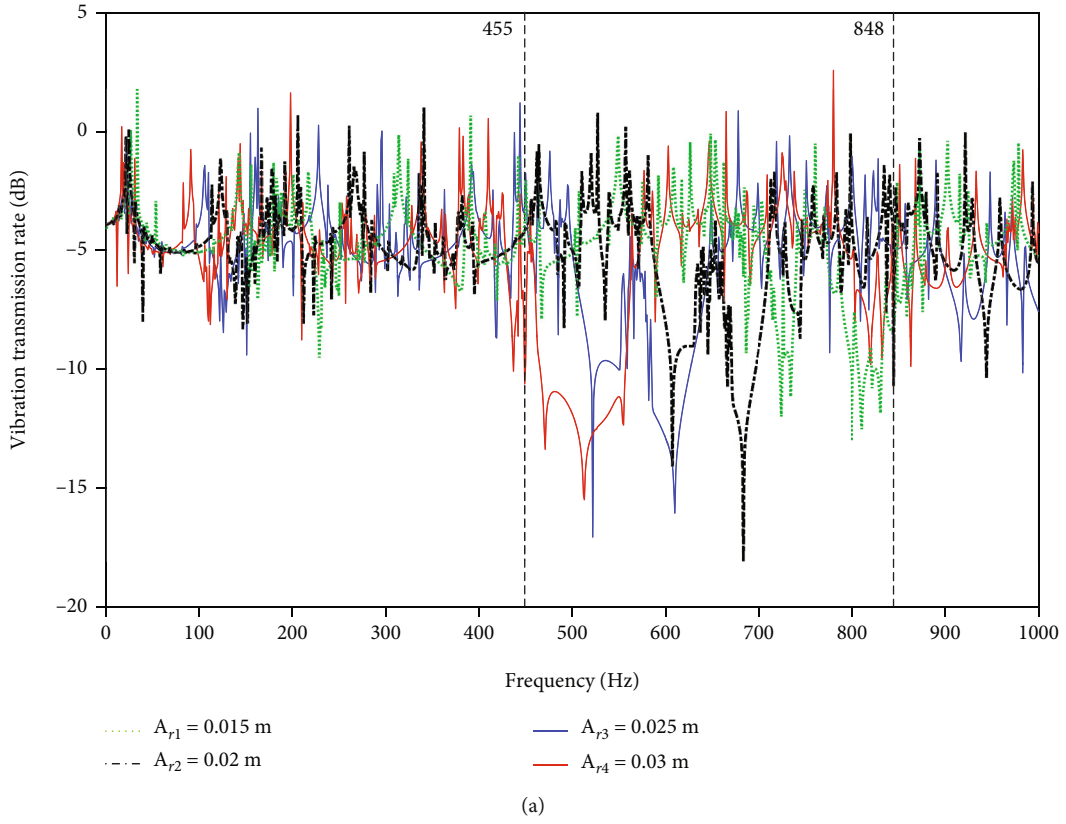

Figure 8: Corresponding to the change of the aluminum alloy section radius: (a) vibration transmission rate of node R; (b) the first band gap.

The structure formed by extending the super element along one dimension is shown in Figure 4. The displacement excitation is applied at node P along the positive y-axis. The y-axis vibration transmission rate of node R is solved and shown in Figure 5.

It can be seen that the vibration transmission rate of node R is attenuated sharply from 455 Hz to 564 Hz, and this frequency range is called as a band gap. The depth of band gap is the value at which the vibration transmission rate within the band gap is the largest, as shown in Figure 5. As

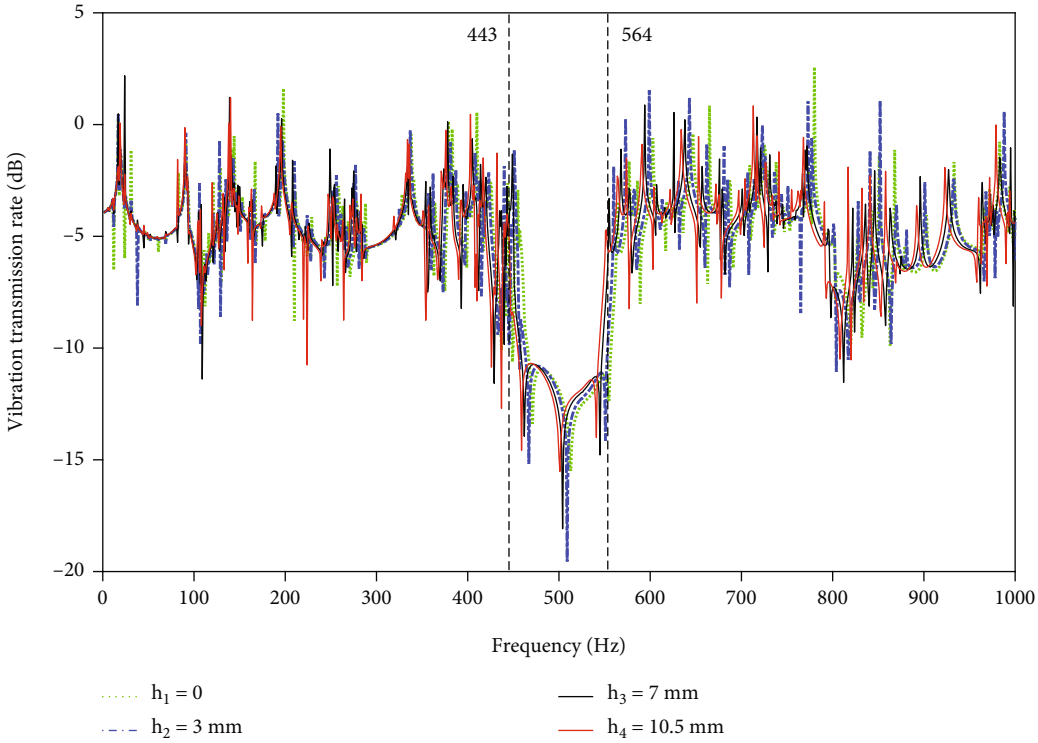

Figure 9: Vibration transmission rate of node R corresponding to the changes in the thickness of the embedded part.

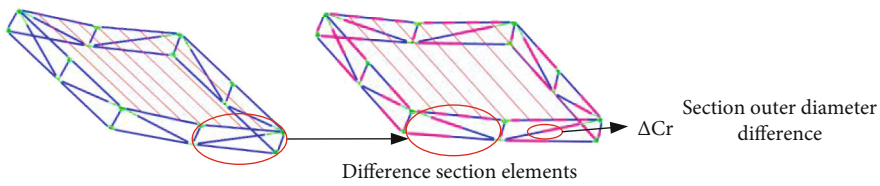

Figure 10: The super element composed of two different sections of carbon fiber tube elements.

the number of super elements is increased from 3 to 6 and 10, the depth is increased by 36.69% and 72.9%, respectively, but the position and width of the band gap are basically the same.

The vibration distributions of the modular space structure at 400 Hz and 500 Hz are shown in Figure 6. It can be seen that the whole structure vibrates at 400 Hz, which means that the elastic wave can move to the far end. However, the vibration at 500 Hz is limited near the excitation source that means the elastic wave can be effectively isolated at the band gap.

5. Optimal Design of the Band Gap of Modular Space Structure

5.1. Sensitivity Analysis. The band gap of the structure may be affected by structural parameters such as element cross-sections, structure size, and cable forces, as shown in Figure 7. The material parameters of the structures in this section are the same as those in Table 1.

At first, the influence of aluminum alloy section radius on the band gap is studied. It can be seen from Figure 8 that when increasing the aluminum alloy section radius Ar by 33.3%, 66.7%, and 100%, the lower limit frequency of the first band gap is decreased by 24.55%, 35.71%, and 40.91%, and the width of the band gap is increased by 69.23%, 97.44%, and 39.74%, respectively. It can be found that with the increase of the aluminum alloy section radius, the band gap shifts towards low frequency, the width of the band gap first increases and then decreases, but the depth is almost not changed. Changes in structural parameters may cause little vibration attenuation between specific frequencies in the band gap, which is called surface localization as shown Figure 8(b). It means the vibration is transmitted with a low attenuation rate in the frequencies.

Then, the aluminum alloy joints are embedded in the carbon fiber beams to form a terminal laminated beam structure. As shown in Figure 9, when the thickness h of the embedded part is set as 0 mm, 3 mm, 7 mm, and

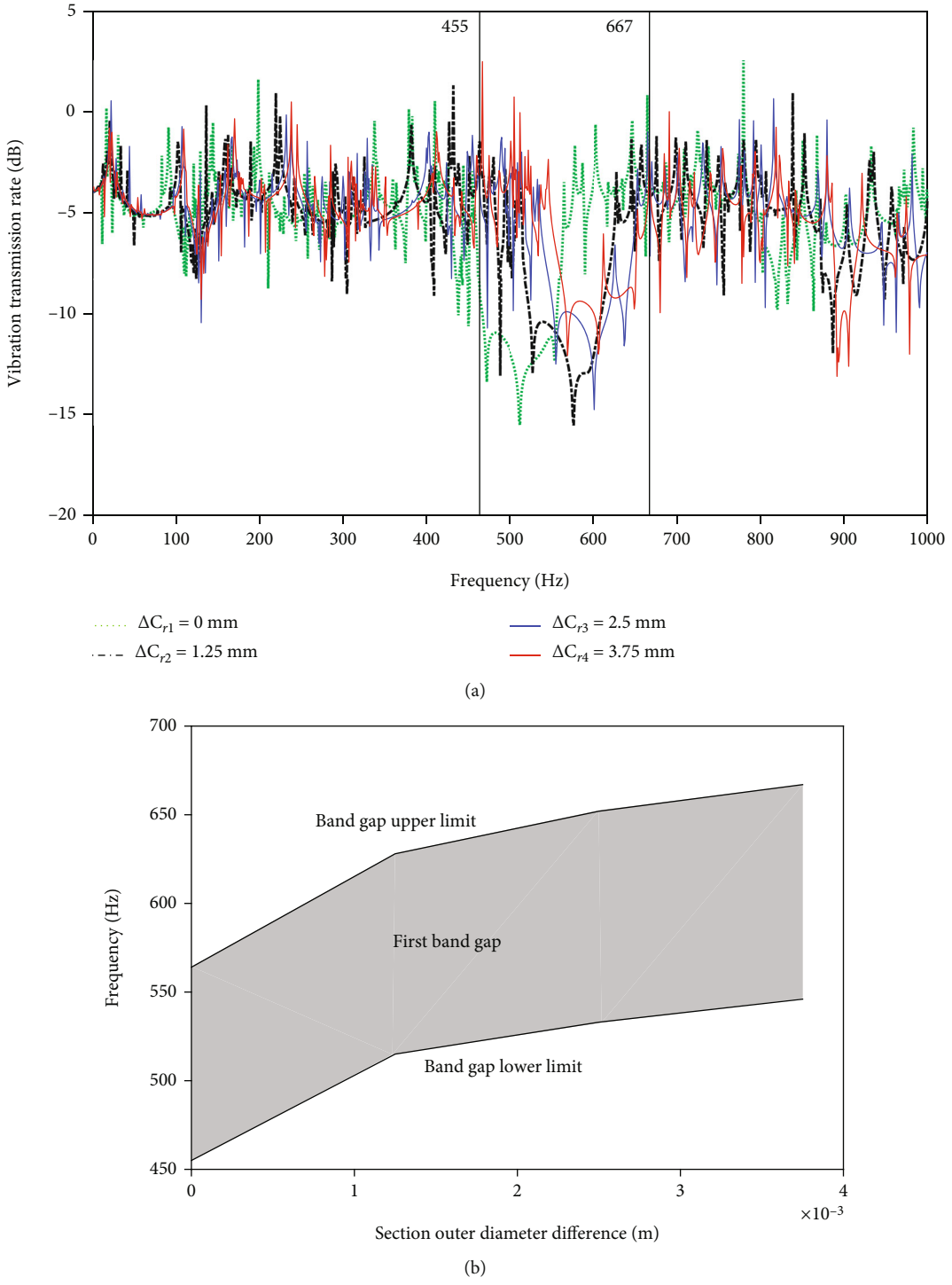

Figure 11: Corresponding to the change of the section outer diameter difference: (a) vibration transmission rate of node R; (b) the first band gap.

10.5 mm, respectively, the band gap will slightly shift towards low frequency, but the width and the depth of the band gap are not changed. The phenomenon may be that the equivalent stiffness of the embedded part is much more minor than the stiffness of the aluminum alloy joint, which has little effect on the band gap.

As shown in Figure 10, the carbon fiber tube is designed as two different section elements. As shown in Figure 11, when the mean value of the outer diameters is set as 0.015 m, 0.0156 m, and 0.0169 m, the difference ΔC_r is set as 0 mm, 1.25 mm, 2.5 mm, and 3.75 mm, respectively. The lower limit frequency of the first band gap is increased by

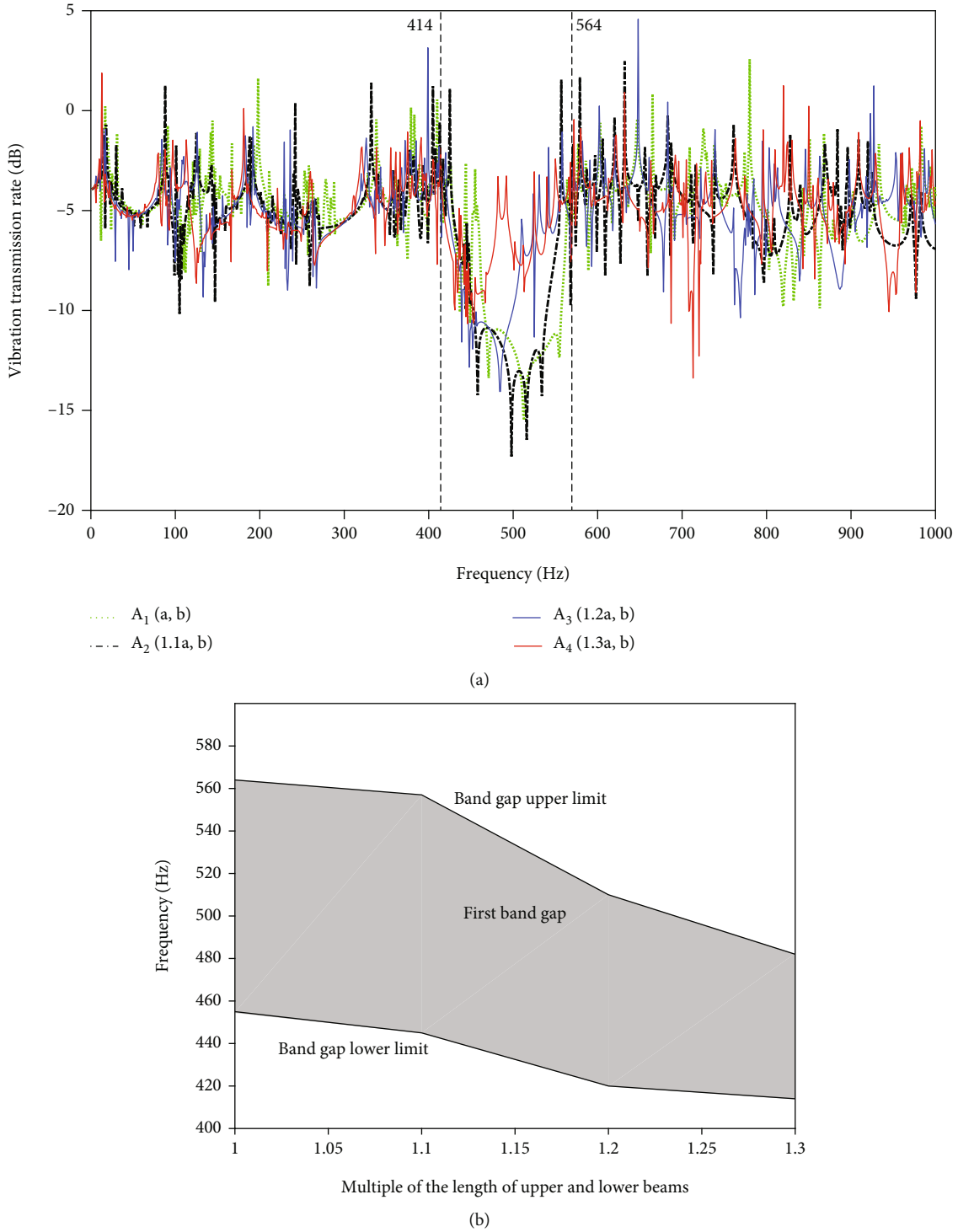

Figure 12: Corresponding to the change of the length of upper and lower chord beams: (a) vibration transmission rate of node R; (b) the first band gap.

13.19%, 17.14%, and 20.00%, and the width of the band gap is increased by 3.67%, 9.17%, and 11.01%, respectively. It can be found that with the increase of the difference ΔC_r, the band gap will gradually shift towards high frequency, the first band gap width increases, and the depth steadily decreases.

As shown in Figure 12, when the length of the upper beams and the lower beams is synchronously increased by 10%, 20%, and 30%, respectively, the lower limit frequency of the first band gap is decreased by 2.20%, 7.69%, and 9.01%, respectively, and the width of the band gap is increased by 2.75%, -19.43%, and -38.53%, respectively. It

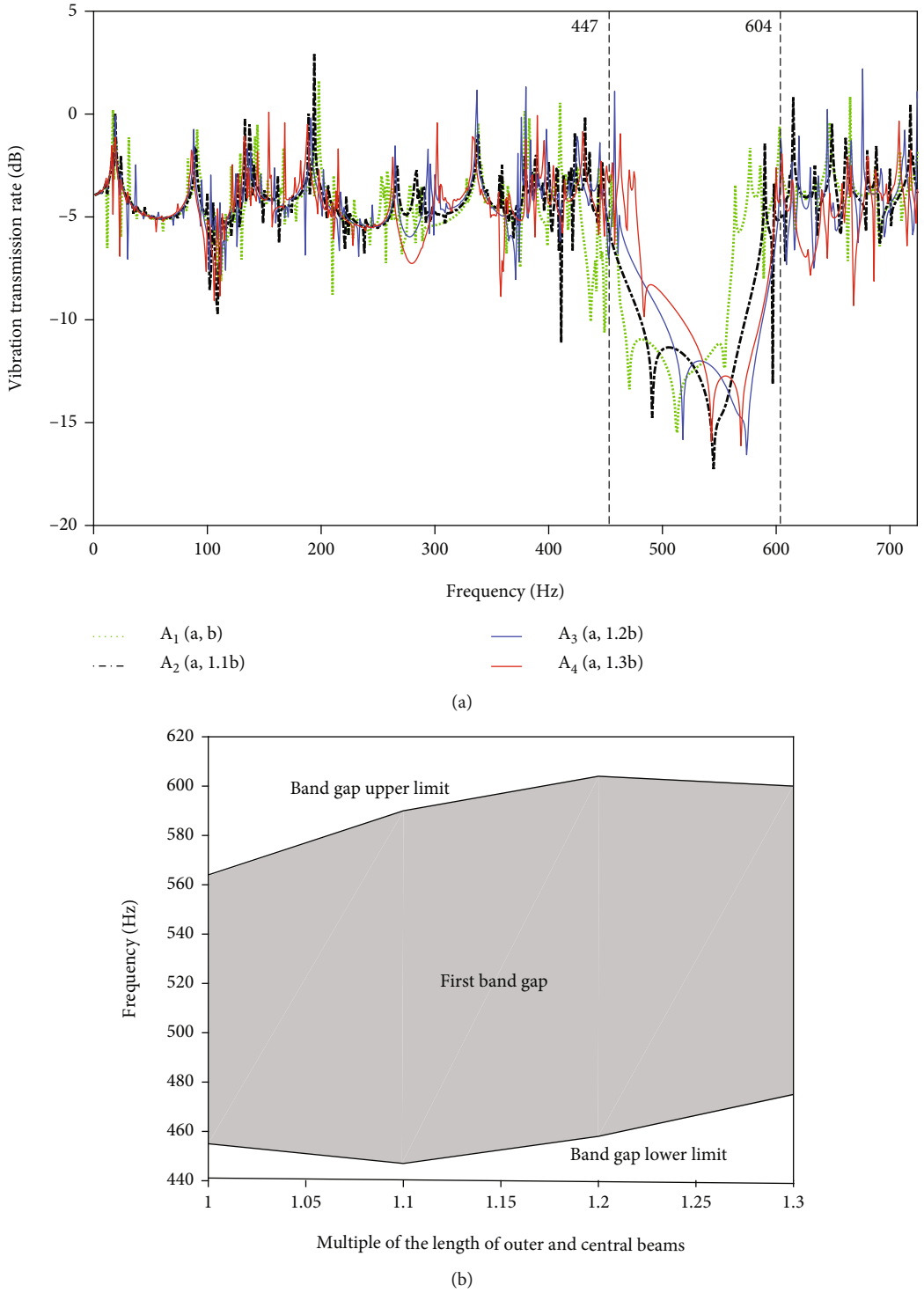

Figure 13: Corresponding to the change of the length of outer beams and center beams: (a) vibration transmission rate of node *R*; (b) the first band gap.

can be found that with the increase of the length of the upper beams and the lower beams, the band gap will shift towards low frequency, the first band gap width first increases and then decreases, and the depth is gradually decreased.

As shown in Figure 13, when the lengths of the outer beams and center beams are synchronously increased by 10%, 20%, and 30%, respectively, the lower limit frequency of the first band gap is decreased by 1.76%, -0.66%, and -4.40%, respectively, and the width of the band gap is

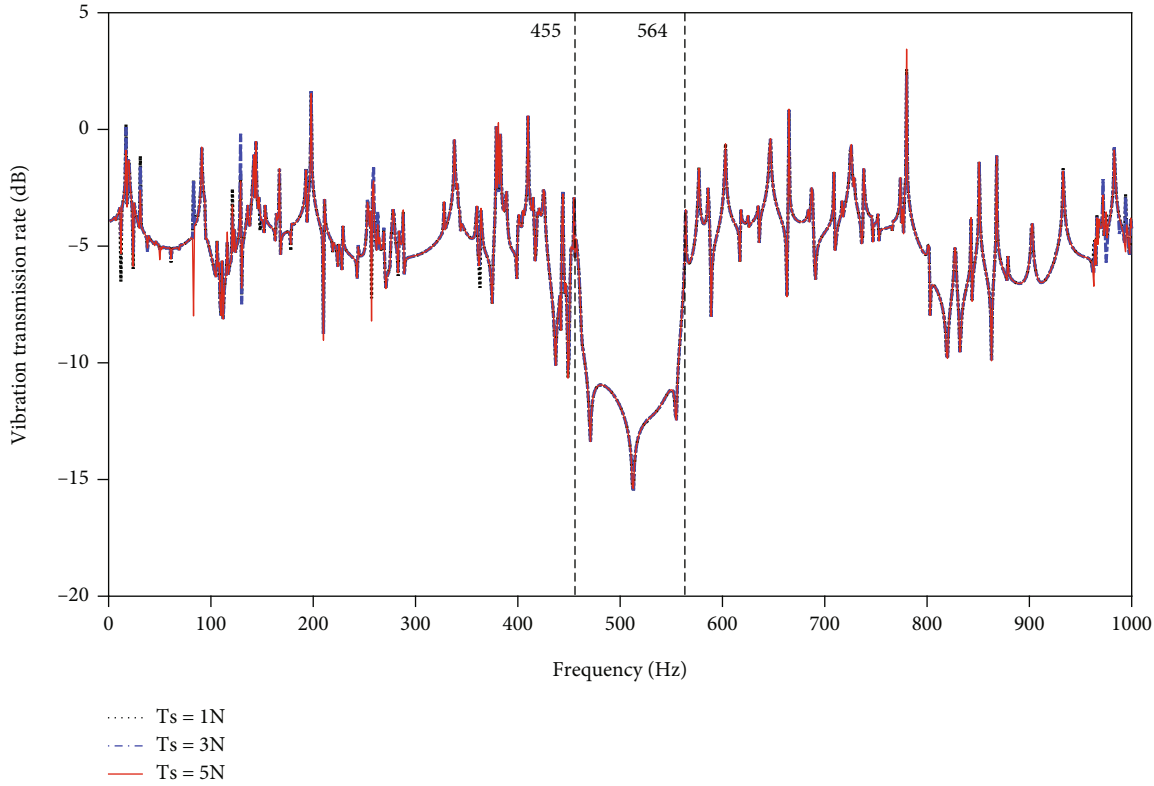

Figure 14: The vibration transmission rate of node R corresponding to the change of cable pretension.

increased by 31.19%, 33.94%, and 14.68%, respectively. It can be found that with the increase of the lengths of the outer beams and center beams, the band gap does not move substantially, the width of the band gap has a significant change, and its value first increases and then decreases, and the depth is gradually increased.

As shown in Figure 14, when the cable pretensions Ts are set as 1 N, 3 N, and 5 N, respectively, the vibration amplitudes of the modular space structure at low frequencies are changed slightly. However, the position, the width, and the depth of the band gap are not changed. The reason is as follows. According to Bloch's theorem, the band gap of the structure is mainly related to the wave number k (i.e., the material parameter of the structure) and the effective length. The cable pretension can affect the structural parameters to a certain extent, thus affecting the wave number k. So, it was considered a factor in the sensitivity analysis. However, it has little effect on the band gap due to the low pretension of the cable in the deployable space structure.

5.2. Optimization Design. The above analysis illustrates that we can optimize the aluminum alloy section radius, the lengths of the upper and lower beams, and the lengths of the central and outer beams to change the position and the width of the band gap. In order to improve the wave isolation characteristics of the modular space structure, we comprehensively consider the influence of these parameters and establish the following band gap optimization model with the ratio of the lower limit of the band gap to the width as the objective function. In addition, to ensure that the change of component size has little effect on the structure's overall size change, the beam length's value range is selected to be between 1 and 1.1 of the original length. The value range of the joint radius is between 1 and 1.5 of the original size.

$$\begin{aligned} &\text{Find } L = \{(1+a)L_1\ (1+b)L_2\ r\}, \\ &\min \quad RB = \frac{f_1}{f_2 - f_1} \\ &\text{s.t.} \begin{cases} a \in [0,0.1] \\ b \in [0,0.1] \\ L_1 = 0.126\,\text{m} \\ L_2 = 1.114\,\text{m} \\ r \in [0.03,0.045]. \end{cases} \end{aligned} \tag{22}$$

where L_1 represents the length of the upper and lower chord beams, L_2 represents the length of the outer and central beams, r is the section radius of the aluminum alloy joints, f_1 is the lower limit of the band gap, and f_2 is the upper limit of the band gap.

The calculation process of the optimization algorithm is shown in Figure 15. Firstly, the optimization variables

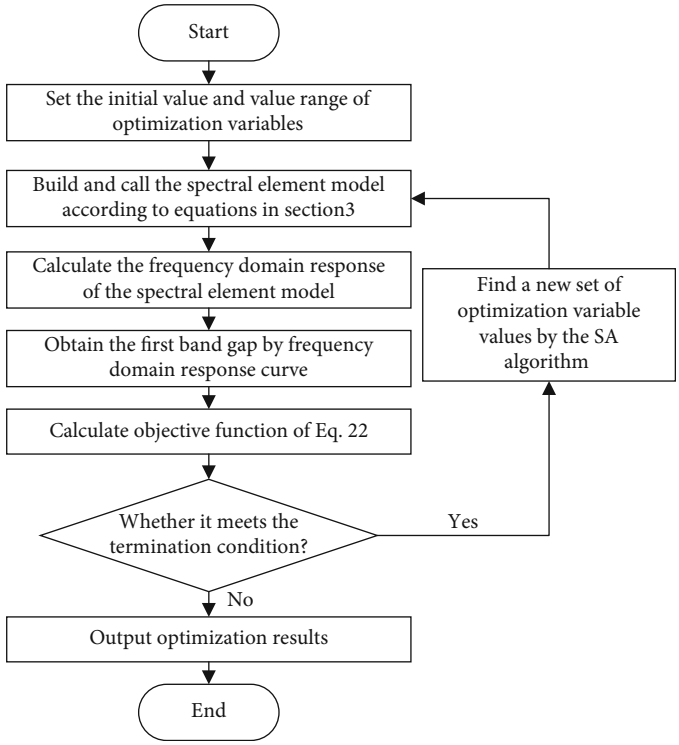

Figure 15: Optimization algorithm flow chart.

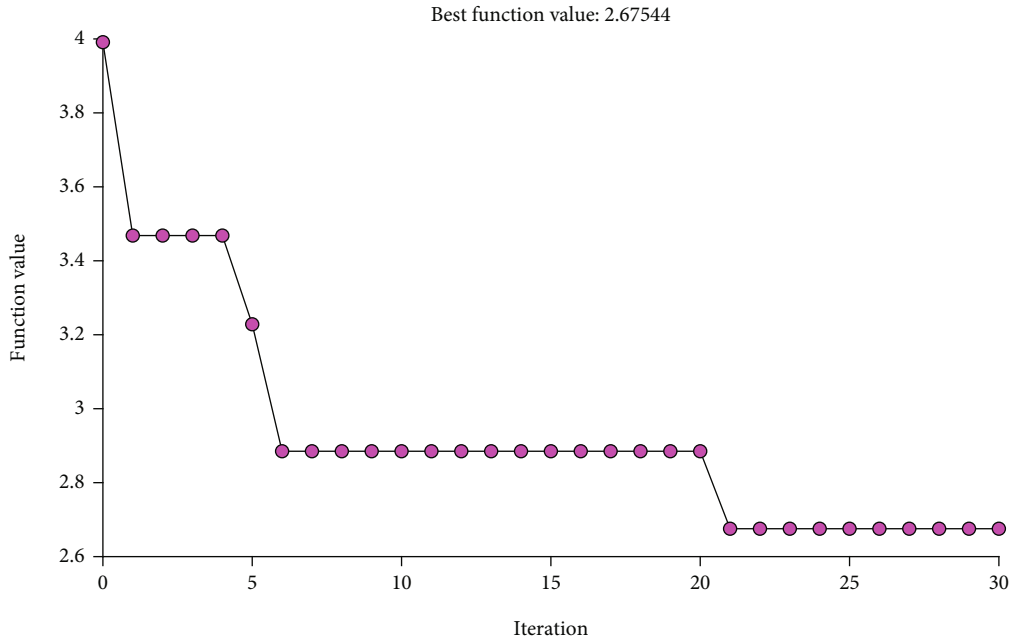

Figure 16: Relative bandwidth optimization iterative process.

are brought into the spectral element model in Section 3, and the frequency-domain response curve of the model is calculated. Then, the first band gap information of the structure is obtained through the frequency domain response curve, including the bandwidth and the lower limit frequency of the band gap. Next, the objective function is calculated by Equation (22) and returned to the SA algorithm to obtain a new set of optimization variable values. Repeat the above process until it satisfies the optimization termination condition and outputs the result.

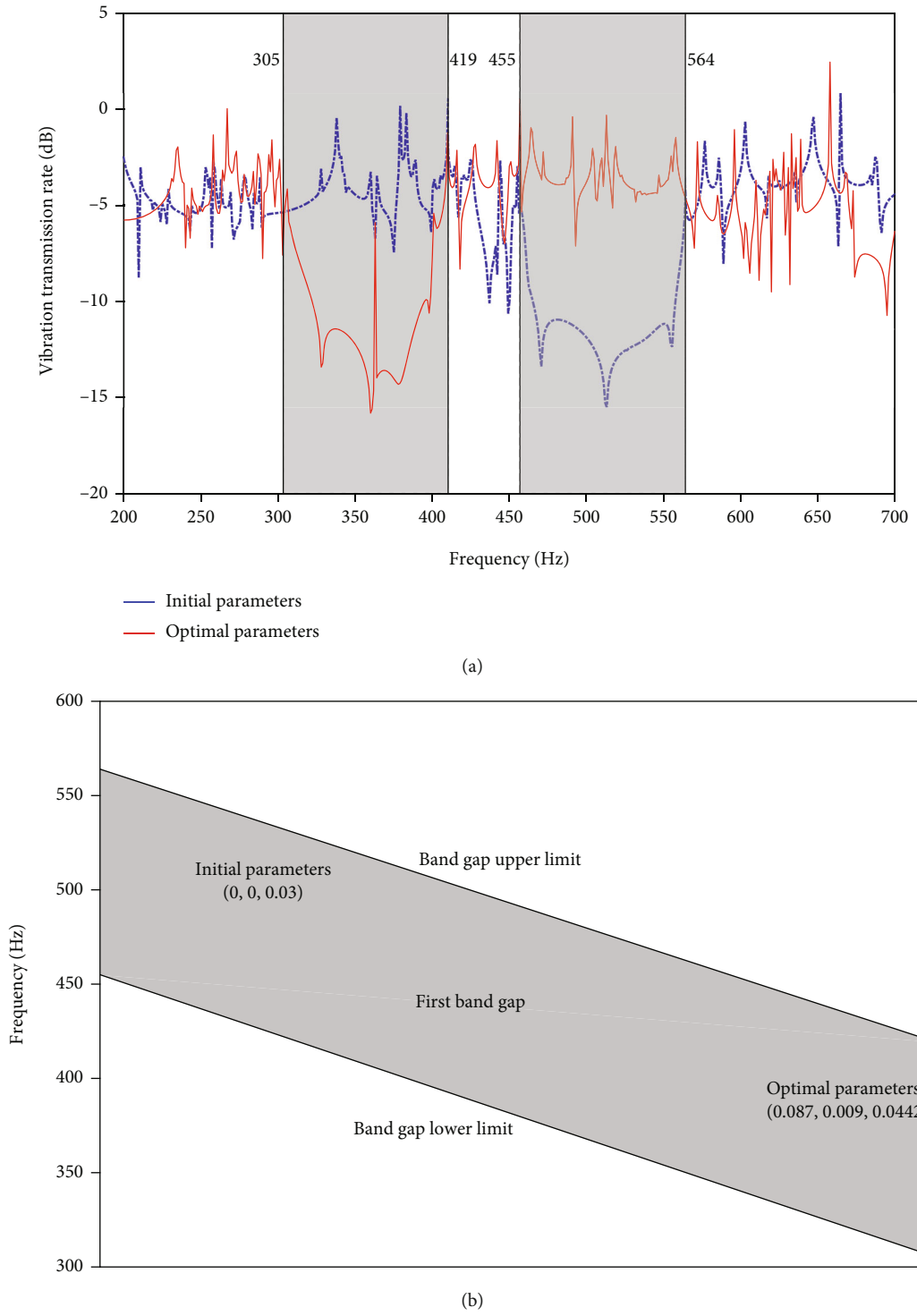

Figure 17: Corresponding to initial parameters and optimal parameters: (a) vibration transmission rate of node R; (b) the first band gap.

For the optimization model of Equation (22), obtaining the optimal global solution is considered at first. In addition, the computational efficiency of the algorithm is considered. The simulated annealing algorithm can obtain the optimal global solution of the optimization model without falling into the optimal local solution. The method also has high computational efficiency. Therefore, the optimization model is solved by the simulated annealing algorithm. The initial parameters are set as [0,0,0.03]. Figure 16 shows that the optimal result can be obtained after 30 iterations. At this time, the optimal length of the upper and lower beams and the central and outer beams and the optimal radius of the aluminum alloy joint are $1.087L_1$, $1.009L_2$, and 0.0442 m, respectively. In this case, the band gap is shifted to the low frequency as shown in Figure 17. It is illustrated that optimization of the

structural parameters can significantly change the position of the band gap.

6. Conclusions

This paper studies a passive vibration control analysis of the modular space structure based on band gap design. Through the band-gap sensitivity analysis of the modular space structure, some key influence factors on the band gap are firstly illustrated. And then, a band gap optimization model is established to improve the wave isolation characteristics of the modular space structure. According to the simulation results, some conclusions can be summarized as follows:

(a) The band gap exists in modular space structures. As the number of basic units increases, the vibration transmission rate of the modular space structure will be decreased

(b) The position and the width of the band gap are greatly influenced by structural parameters, including the aluminum alloy section radius, the length of the upper and lower beams, and the length of the central and outer beams

(c) The elastic wave in the band gap can be effectively isolated, and manual optimization of the structural parameters can significantly change the position of the band gap. That is to say, wave isolation characteristics of the modular space structure can be improved by optimizing the structural parameters

Data Availability

The data used to support the findings of this study are available from the corresponding author upon request.

Conflicts of Interest

The authors declare that they have no conflicts of interest.

Acknowledgments

The project is supported by the National Natural Science Foundation of China (Grant Nos. 51775403 and 51905401), the Fundamental Research Funds of Xidian University (Grant No. JB210415), and the Key Research and Development Program of Shaanxi (Program No. 2022GY-314).

References

[1] F. Hu, Y. P. Song, Y. D. Xu, and H. Wen, "Synthesis and optimization of modular deployable truss antenna reflector," *Aircraft Engineering and Aerospace Technology*, vol. 90, no. 8, pp. 1288–1294, 2018.

[2] J. C. Chen, Y. Zhang, L. W. Wu, T. You, and X. Ning, "An adaptive clustering-based algorithm for automatic path planning of heterogeneous UAVs," *IEEE Transactions on Intelligent Transportation Systems*, pp. 1–12, 2021.

[3] J. Chen, C. Du, Y. Zhang, P. Han, and W. Wei, "A clustering-based coverage path planning method for autonomous heterogeneous UAVs," *IEEE Transactions on Intelligent Transportation Systems*, pp. 1–11, 2021.

[4] J. C. Chen, Y. He, Y. Zhang, P. Han, and C. Du, "Energy-aware scheduling for dependent tasks in heterogeneous multiprocessor systems," *Journal of Systems Architecture*, vol. 129, article 102598, 2022.

[5] J. C. Chen, F. Y. Ling, Y. Zhang, T. You, Y. Liu, and X. Du, "Coverage path planning of heterogeneous unmanned aerial vehicles based on ant colony system," *Swarm and Evolutionary Computation*, vol. 69, article 101005, 2022.

[6] Y. Liu, K. Zhang, W. Z. Zhang, and X. Y. Meng, "Wave-based vibration control of large cable net structures," *Wave Motion*, vol. 77, pp. 139–155, 2018.

[7] Y. Zhao, Y. Y. Wang, and W. L. Ma, "Active control of power flow transmission in complex space truss structures based on the advanced Timoshenko theory," *Journal of Vibration and Control*, vol. 21, no. 8, pp. 1594–1607, 2015.

[8] Y. Q. Tang, T. J. Li, Q. Lv, and X. Wang, "A self-vibration-control tensegrity structure for space large-scale construction," *Mechanical Systems and Signal Processing*, vol. 177, article 109241, 2022.

[9] J. A. Bishop and A. G. Striz, "On using genetic algorithms for optimum damper placement in space trusses," *Structural and Multidisciplinary Optimization*, vol. 28, no. 2, pp. 136–145, 2004.

[10] R. Xu, D. X. Li, Q. Luo, W. Liu, and J. Jiang, "Microvibration suppression of space truss structures using viscoelastic dampers with design parameter optimization," *Proceedings of the Institution of Mechanical Engineers Part G-Journal of Aerospace Engineering*, vol. 230, no. 3, pp. 539–553, 2016.

[11] I. H. Kim, H. J. Jung, and J. T. Kim, "Numerical investigation of an MR damper-based smart passive control system for mitigating vibration of stay cables," *Structural Engineering and Mechanics*, vol. 37, no. 4, pp. 443–458, 2011.

[12] X. Tong and X. W. Zhao, "Passive vibration control of the SCOLE beam system," *Structural Control and Health Monitoring*, vol. 25, no. 8, article e2204, 2018.

[13] A. Preumont, B. de Marneffe, A. Deraemaeker, and F. Bossens, "The damping of a truss structure with a piezoelectric transducer," *Computers and Structures*, vol. 86, no. 3-5, pp. 227–239, 2008.

[14] Y. R. Teo and A. J. Fleming, "Optimal integral force feedback for active vibration control," *Journal of Sound and Vibration*, vol. 356, pp. 20–33, 2015.

[15] B. Agrawal, "Jitter control for imaging spacecraft," in *2009 4th International Conference on Recent Advances in Space Technologies*, pp. 615–620, Istanbul, Turkey, 2009.

[16] V. S. Sorokin and J. J. Thomsen, "Effects of weak nonlinearity on the dispersion relation and frequency band gaps of a periodic Bernoulli-Euler beam," *Mechanical Systems and Signal Processing*, vol. 472, no. 2186, article 20150751, 2016.

[17] X. Zhaowang, X. Xiangxi, J. Fuyu, W. Zongyao, L. Zhiwei, and C. Rui, "Study on vibration characteristics of periodic truss structure of offshore platform," *Advances in Mechanical Engineering*, vol. 12, no. 11, Article ID 168781402097288, 2020.

[18] J. Q. Li and H. J. Shen, "Analysis of longitudinal vibration band gaps in periodic carbon nanotube intramolecular junctions using finite element method," *AIP Advances*, vol. 5, no. 12, 2015.

[19] X. Q. Zhou, D. Y. Yu, X. Y. Shao, S. Wang, and Y. H. Tian, "Band gap characteristics of periodically stiffened-thin-plate based on center- finite-difference-method," *Thin-Walled Structures*, vol. 82, pp. 115–123, 2014.

[20] Y. Z. Wang, F. M. Li, K. Kishimoto, Y. S. Wang, and W. H. Huang, "Wave band gaps in three-dimensional periodic piezoelectric structures," *Mechanics Research Communications*, vol. 36, no. 4, pp. 461–468, 2009.

[21] T. Li, X. Ma, Q. Zhang, and Z. Wang, "Band gap properties of periodic tapered beam structure using traveling wave method," *Journal of Theoretical and Applied Mechanics*, vol. 54, no. 4, pp. 1297–1308, 2016.

[22] V. Ferrando, J. C. Castro-Palacio, B. Marí, and J. A. Monsoriu, "Study on band gap structure of Fibonacci quantum superlattices by using the transfer matrix method," *Modern Physics Letters B*, vol. 28, article 1450053, no. 7, 2014.

[23] Z. J. Wu, Y. Z. Wang, and F. M. Li, "Analysis on band gap properties of periodic structures of bar system using the spectral element method," *Waves in Random and Complex Media*, vol. 23, no. 4, pp. 349–372, 2013.

[24] Y. Tang, X. Wang, X. Zhou, and T. Liu, "A simple wave/power flow analysis method for vibration control of large cable-frame structures," *Journal of Vibration and Control, online*, vol. 28, no. 17-18, pp. 2319–2332, 2022.

[25] Z. J. Wu, F. M. Li, and C. Z. Zhang, "Vibration band-gap properties of three-dimensional Kagome lattices using the spectral element method," *Journal of Sound and Vibration*, vol. 341, pp. 162–173, 2015.

[26] Z. Zhang, T. J. Li, Z. W. Wang, and Y. Tang, "Band gap characteristics of flexural wave of two-dimensional periodic frame structure composed of locally resonant composite beam," *Mechanical Systems and Signal Processing*, vol. 131, pp. 364–380, 2019.

[27] U. Lee and J. Lee, "Dynamic continuum modeling of truss-type space structures using spectral elements," *Journal of Spacecraft and Rockets*, vol. 33, no. 3, pp. 404–409, 1996.

[28] M. Dutkiewicz and M. Machado, "Spectral element method in the analysis of vibrations of overhead transmission line in damping environment," *Structural Engineering and Mechanics*, vol. 71, no. 3, pp. 291–303, 2019.

[29] B. Jeong, T. Kim, and U. Lee, "Vibration analysis of a multi-span beam subjected to a moving point force using spectral element method," *Structural Engineering and Mechanics*, vol. 65, no. 3, pp. 263–274, 2018.